Proton acceleration from microdroplet spray by weakly relativistic femtosecond laser pulses

Xiao-Yu Peng,[1,2] Jie Zhang,[1,*] Jun Zheng,[1] Zheng-Ming Sheng,[1] Miao-Hua Xu,[1] Zhi-Yuan Zheng,[1] Tian-Jiao Liang,[1] Yu-Tong Li,[1] Quan-Li Dong,[1] Xiao-Hui Yuan,[1] Ying-Jun Li,[1,2] and Han-Ming Li[1,2]

[1]*Key Laboratory of Optical Physics, Institute of Physics, Chinese Academy of Sciences, Beijing 100080, People's of Republic, China*

[2]*Department of Physics, China University of Mining & Technology, Beijing 100083, People's of Republic, China*

(Received 27 May 2006; revised manuscript received 25 July 2006; published 26 September 2006)

Angular distribution of protons is measured from ethanol droplet spray irradiated by linearly polarized 150 fs laser pulses at an intensity of 1.1×10^{16} W/cm^2. Fast protons (with energies >16 keV) with an anisotropic distribution can be observed only in or near the polarization plane of the laser fields, while the slow protons (with energies $\leqq16$ keV) emit with nearly an isotropic distribution. Two-dimensional particle-in-cell simulations suggest that three groups of protons originate from different acceleration regimes in the laser-droplet interaction. The first group with the highest energies is accelerated backwards by the anisotropic charge-separation field near the front surface (laser-droplet interaction side) due to the resonance absorption; the second group (forward emission) is generated by the target-normal sheath acceleration mechanism; and the third group, with the lowest energies, is accelerated by the hydrodynamic expansion of the droplet plasmas.

DOI: 10.1103/PhysRevE.74.036405 PACS number(s): 52.38.Kd, 52.65.−y, 52.70.Nc

I. INTRODUCTION

The acceleration of energetic ions to high energies within a very short distance in the interactions of short intense laser pulses with a variety of targets has been widely investigated in recent years [1–9] to the end of the development of compact ion sources with a well-characterized emission for various applications [10–13].

The mechanisms for ion (include the protons) acceleration in the laser-plasma interactions depends on the duration, intensity, and polarization of laser pulses and also is related with density scale lengths of plasmas and target configurations [14]. For the long pulse case, the acceleration of ions was interpreted as the isothermal expansion of plasmas in the process of the laser energy absorption in targets [15]. For the ultrashort pulse ($\leqslant1$ ps) and relativistic intense ($I\geqslant1.38\times10^{18}$ W/cm^2) case using thin foil targets, two mechanisms play dominant roles in the ion acceleration. Firstly the pondermotive charge separation at the irradiated surface induces a double layer and the resulting static fields accelerate ions into the target [16,17]; secondly the laser-heated electrons propagate through the target, building up a space charge at the rear surface and extract ions by the target-normal sheath acceleration (TNSA) mechanism [1,18,19]. As for cluster targets irradiated by intense laser pulses, electrons can be expelled, and then the ions can be accelerated to high energies with a nearly isotropic distribution in the 4π space by the Coulomb explosion [20]. If the size of clusters is large enough, the ions can also be accelerated by the hydrodynamic expansion [21].

Due to the advantages of low-debris and easy availability, droplet targets are suitable for a reliable operation of ion sources and have attracted attention in recent years [6,22,23]. In these experiments [6,22], large droplet targets with diameters approximately equal to or much larger than the focal spot size of the laser beam are used. In this case, the spherical surface of these large droplets play a small role in the interaction because the laser beam is focused on the surface of the droplet as a laser beam is focused on a bulk foil target. In some experiments [23], small droplets with a diameter much less than the focal spot size of the laser beam were used as targets. In this case, the incident angle of the laser beam irradiating on the front surface of the droplets increases continuously from 0 to ±90°, thus making this kind of target very suitable for the study of the mechanisms of particle acceleration. However, there have been only a few publications concentrated in the study of the proton generation from the small droplets, and in particular, direct measurements of the angular distributions of protons under the irradiation of femtosecond laser beam have not been reported. The physics process of laser particle acceleration is far from understood in this case.

In this paper, we directly measure the angular distributions of protons from few-microns ethanol droplets irradiated by linearly polarized 150 fs laser pulses at an intensity about 1.1×10^{16} W/cm^2. These measurements can help us understand the mechanisms of the ion (proton) acceleration under the irradiation femtosecond laser pulses.

II. EXPERIMENTAL SETUP

The experiments were carried out at the Laboratory of Optical Physics at the Institute of Physics with a Ti:sapphire chirped pulse amplification (CPA) laser system operating at a wavelength around 790 nm at a repetition rate of 10 Hz. The experimental setup is similar as described in Ref. [24]. The laser delivered 5.2 mJ energy in 150 fs pulses with a peak-to-pedestal contrast ratio of 10^5 at about 20 ps before the peak measured by a third-order autocorrelator. A linearly polarized laser beam was focused with an 80 mm focal length lens, yielding a peak intensity around 1.1×10^{16} W/cm^2 at the focus with a diameter of about 20 μm. The electric field vector of the laser beam was parallel or perpendicular to the horizontal plane by rotating a half-wave plate.

*Corresponding author. Email address: jzhang@aphy.iphy.ac.cn

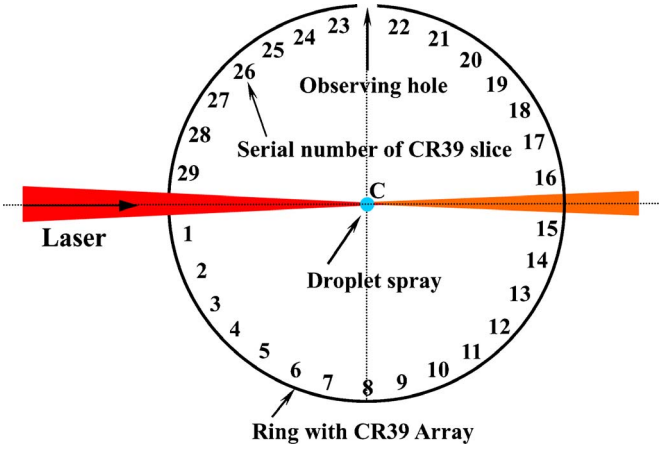

FIG. 1. (Color online) Sketch map of the CR39 array attached on inner wall of the ring.

A solenoid-driven pulsed valve with a 500-μm orifice was used to generate ethanol droplets under a backing pressure of 2 MPa. The mean size of the droplets was about 4–5 microns, about 1/5 the size of the focus. The number density of the spray at 1 mm under the orifice (the focusing position) was about 7.9×10^8 droplets/cm^3. The temperature of the valve was about 300 K.

The angular distribution of the ion emission was measured with an array of CR39 plastic nuclear track detectors (products of SY-1, Japan) attached on a ring. Each slice of the detector has a size of 5×5 mm^2 with a thickness of 1 mm. In order to conveniently analyze the angular distribution of ions, the same procedures as described in Ref. [24] were taken to ensure the laser light was focused exactly at the center of the droplet spray at about 1 mm under the orifice so that the angular distribution of ions would be symmetric respect to the propagation of the laser axis. Twenty-nine slices of CR39 detectors were used to cover nearly all the inner walls of the ring except the passage of the laser beam and an observation hole in the direction of 90°. The angular resolution is about 10°. The schematic of the array of CR39 detectors is shown in Fig. 1. All the CR39 detectors were etched for about 2 h in the same sodium hydroxide solution simultaneously. The ion tracks of different CR39 detectors were observed and recorded by a charge-coupled device (CCD) camera under a microscope with the same magnification.

An ethanol molecule has three kinds of atoms: H, C, and O. All these atoms can be accelerated. However, protons would be preferentially accelerated due to their high charge-to-mass ratio and subsequently shield heavier ions from the electric field. The intensity (1.1×10^{16} W/cm^2) of the laser beam used in our experiments is much less than the relativistic intensity (1.38×10^{18} W/cm^2). At such condition, all ions could be accelerated to only moderate energies. In addition, since the carbon and oxygen ions have a much larger energy loss rate in the CR39, this results in different track growth characteristics from protons [25,26]. Although in a few cases the maximum carbon energy was as large as half of the maximum proton energy, the flux was much lower, and no more than 10% of the energy was contained in nonhydrogenic ions above 100 keV [27]. This means that the protons mainly contributed to the ion tracks recorded by CR39 detectors, i.e., the ion emission would be predominantly from protons.

III. EXPERIMENTAL RESULTS

Figure 2 shows typical images of proton tracks and their angular distributions relative to the laser axis. The results were accumulated over 24 000 shots. Firstly we measured the angular distribution of protons in the polarization plane of the laser beam. We found that there were not only backward emissions but also lateral and forward protons emissions. However, the proton tracks of backward emissions are stronger and more distinct than those of the forward emission. Many weak tracks can also be observed on each slice of CR39 detectors. Figure 2(a) shows a typical magnified image of the proton tracks at the strongest emission direction taken by the CCD camera fixed on the microscope. By setting a reading threshold value to count the number of distinct tracks of protons and reading out the densities of the distinct tracks, we got the angular distributions of protons in Fig. 2(b). From Fig. 2(b) we found that the distribution is anisotropic. The proton track density of each slice of CR39 detector ranges from 6.1×10^3 mm^{-2} to 1.3×10^6 mm^{-2} (note that those weak tracks corresponding to ions with much lower energies were not counted). The strongest emission direction locates at the angle near ±105° in the back emission relative to the laser propagation direction. In addition, we also observed that there are two small but not very distinct "jets" in the forward emission from Fig. 2(b).

When the laser-polarization direction was changed to be perpendicular to the horizontal plane (also is the plane of the ring) by rotating the half-wave plate, no distinct tracks as in Fig. 2(b) were observed. There are only very weak and very small tracks on each slice. This means that these tracks were produced by some protons with much smaller energies than those observed in the polarization plane of the laser field. To distinguish these protons from those with higher energies (we call them "fast protons") mentioned in Figs. 2(a) and 2(b), we call these population "slow protons." It is difficult to observe and read these very weak tracks. In order to get a higher contrast to count them, we adjusted the microscope and deliberately got a virtual image of these weak tracks. Thus, these weak tracks shown in Fig. 2(c) look like white dots rather than black dots as shown in Fig. 2(a). Using this method we can easily identify even the very weak and very small tracks formed by the slow protons. By setting a new reading threshold value to take nearly all count of these weak tracks of protons and reading out the densities of these tracks, we got the angular distribution of these slow protons shown in Fig. 2(d). From Fig. 2(d), we can see that this distribution is nearly isotropic. The track density of slow protons on each slice of CR39 detectors fluctuates from 6.0×10^3 mm^{-2} to 8.0×10^3 mm^{-2} at a mean value of about 7.0×10^3 mm^{-2}. In fact, such very weak and small tracks could be observed not only on each slice of CR39 detectors in Fig. 2(c) but also on each slice of CR39 detectors in Fig. 2(a). This indicates that these slow protons are independent

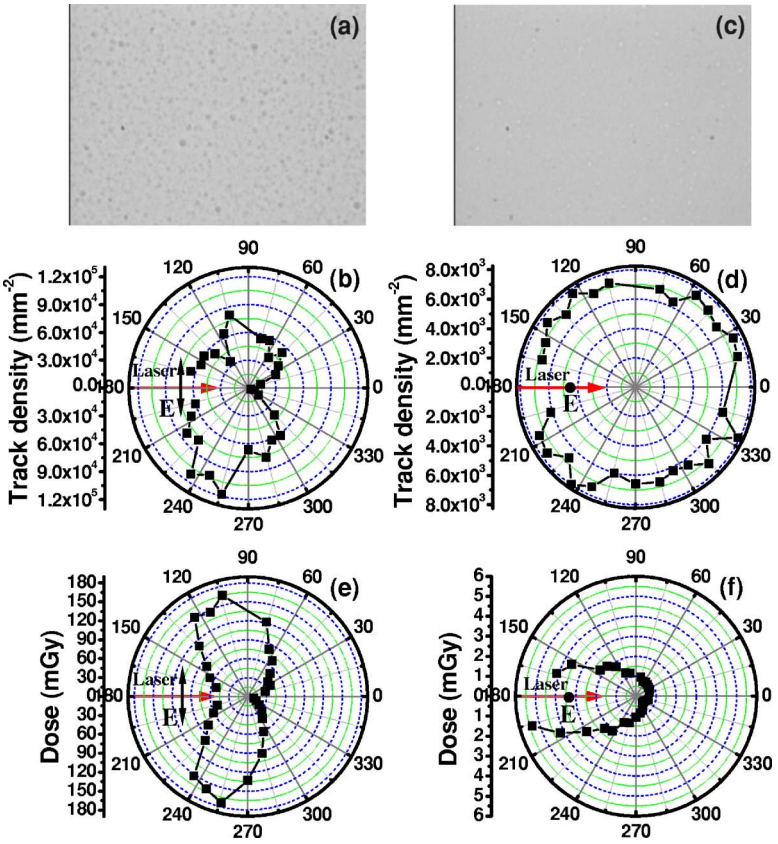

FIG. 2. (Color online) The typical image of the fast proton tracks (a), their angular distributions in the polarization plane of the laser light (b), the typical image of the slow proton tracks (c), and their angular distributions in the plane perpendicular to the polarization plane of the laser light (d). Frames (e) and (f) are the corresponding distributions of hot electrons under the same experimental conditions in (b) and (d), respectively.

on the polarization of the incident laser light and emit at all directions in the 4π space, while those fast protons only observed in or near the polarization plane of the incident laser light are strongly dependent on the polarization of the incident laser pulses.

To compare the angular distribution of protons with that of hot electrons, we used the LiF thermoluminescent dosimeter (TLD) detector array attached on the inner wall of the ring (covered by a layer of an aluminum film with a thickness of 20 μm) to measure the angular distributions of hot electrons from the droplets under the same experimental conditions as described above. Figures 2(e) and 2(f) represent the angular distribution of hot electrons with energies over 50 keV in the polarization plane and in the plane perpendicular to the polarization plane of the laser light respectively. From Figs. 2(e) and Fig. 2(f) we can see the two jets of hot electrons only emit in or near the polarization plane and takes on a distinct anisotropic angular distribution just like that of the fast protons in Fig. 2(b). Comparing Fig. 2(b) with Fig. 2(e) we find both the fast protons and the hot electrons have the same directions for the emission peaks at the angle near ±105° relative to the laser-propagation direction. This means that the mechanism of the acceleration of the fast protons is related to that of the generation of the hot electrons. However, comparing Fig. 2(d) with Fig. 2(f) we find there are no relations between the slow protons and the hot electrons. This indicates that the origin of the slow protons differs from that of the fast protons observed in the polarization plane of the laser beam.

In the above experiments, the laser beam was focused at the center of the droplet spray at 1 mm below the orifice in order to obtain a strong emission of protons. If we move the focusing position a little further along the laser axis under the same experimental conditions as in Fig. 2(b), we find that the strongest emission direction of protons changed from several degrees to tens of degrees accordingly. This phenomenon indicates that the pattern of the distribution of the fast protons is sensitive to the focusing position in the droplet spray, similar to that of the hot electrons [28]. However, the movement of the focusing position only changes the angular distributions of protons in the polarization plane to some extent, but does not affect the result that the fast protons emit only in or near the polarization plane, and the angular distributions of fast protons always takes on an anisotropic pattern.

We used a small dipole magnetic spectrometer with low energy resolutions especially designed for our small chamber with a diameter of 20 cm to measure roughly the spectrum of protons at the angle of 45° relative to the laser axis in the polarization plane of the incident laser light. Figure 3 shows the energy spectrum of protons from ethanol droplets using LiF thermoluminescent dosimeter (TLD) detectors under the same conditions as those in Figs. 2(a) and 2(b). We find the peak of the proton spectrum is around 15 keV from Fig. 3. By using a strip CR39 detector to substitute the TLD detectors to compare the tracks on it with those tracks in Fig. 2(c), we can confirm the energy of the slow protons corresponding to the very weak tracks observed in Fig. 2(d) and also in Fig. 2(b) is $\leqslant$16 keV. This threshold energy value (16 keV) can be used as the dividing ridge between the slow protons (with energy $\leqslant$16 keV) and the fast protons (with energy $>$16 keV). The energy of the peak of the proton spectrum

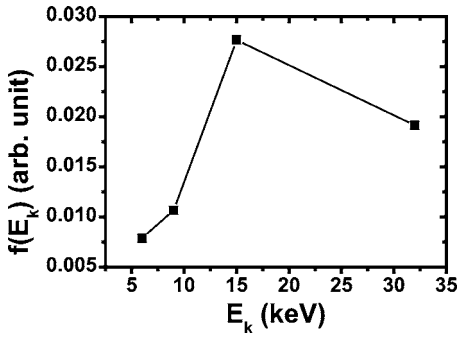

FIG. 3. The rough proton energy spectrum measured in the polarization plane of the laser light by using the TLD detectors.

around 15 keV corresponds to the slow protons observed in Fig. 2(e). This means that the most protons generated in the laser-droplet interaction are slow protons. We can obtain that the maximum energy of fast protons is about 32 keV from Fig. 3. Actually, the data with higher energies over 56 keV are not plotted in this figure because the TLD detectors corresponding to the energies over 56 keV locate near the entrance direction of the magnetic spectrometer and are possibly irradiated by the scattering light from the droplet spray. However, we can observe the signals corresponding to the energy of around 56 keV if we replace the TDL detector in the magnetic spectrometer by a strip CR39 detector that is not sensitive to the visible light. So we believe that the maximum energy of the fast protons is at least more than 56 keV. Another reason why we cannot obtain the maximum energy of the fast protons accurately from this magnetic spectrometer is its very low energy resolution at its high energy end. This means those data over 56 keV are not adoptable in Fig. 3. However, we can estimate roughly the maximum energy of the protons. To estimate the maximum energy of the fast protons, we used a layer of polyimide ($C_{33}H_{24}N_2O_5$) films with a thickness of 1 μm, which corresponds to proton cutoff energy of 70 keV to cover every slice of the CR39 detectors in Fig. 1. But we cannot observe any tracks even the very weak tracks at all on all detectors. The lowest energy which can generate the very weak tracks on CR39 such as those shown in Fig. 2 should be $\geqq \sim 16$ keV according to the above analysis. If we expect the signals (at least the very weak tracks) on CR39 when we use a layer of polyimide film to cover the CR39 detector, the energies of protons should be at least (70 keV+16 keV=86 keV). Thus we can deduce that the maximum energy of the fast protons is less than 86 keV and is in the range of 56 keV to 86 keV. This result is very different from that found in Ref. [23], where the maximum energy of the fast protons is only up to 20 keV under similar experimental conditions.

IV. TWO-DIMENSIONAL PARTICLE-IN-CELL SIMULATIONS AND DISCUSSION

Under the weakly relativistic irradiation of laser beam, the quasistatic field acceleration due to the charge separation by the laser pondermotive force plays a very small role in the acceleration of protons. Our experimental results that the back emission of protons is stronger than that of the forward emission in Fig. 2(b) indicate that the TNSA mechanism is not dominant. A strong anisotropic emission of fast protons indicates that a strong anisotropic accelerating electrostatic-field is formed around the droplet plasmas surface. This field is related with the hot electrons generated mainly by the resonance absorption described in our previous work [24]. The population of slow protons with nearly an isotropic distribution and with no relation with the hot electrons [see Fig. 2(c)] means these slow protons are accelerated by different mechanisms.

Two-dimensional (2D) particle-in-cell (PIC) simulations are performed to explain our experiments. Our main attention is paid to the formation of the electrostatic field responsible for the proton distribution. In the simulations, the spherical droplet plasmas are approximated as infinitely long cylinders for the sake of simplicity. The droplet diameter is smaller than the laser focus diameter so the laser light irradiates all the front surface of the droplet. We take $a_0=0.1$, which corresponds to a laser intensity at the focus used in our experiment. The simulation box size is $40\lambda_0 \times 40\lambda_0$; here, λ_0 is the laser wavelength in vacuum. A *p*-polarized laser pulse with a duration of $60\tau_0$ (τ_0 is the laser cycle in vacuum) is incident along the *x* direction from the left, normally onto the droplet-plasma with a diameter of $5\lambda_0$. Initially the electron density increases exponentially along the radial direction of the droplet from $0.2n_c$ at the droplet edge ($r=2.5\lambda_0$ from the droplet center) until $2.0n_c$ at $r=0.5\lambda_0$, where n_c is the critical density. The electron density remains at $2.0n_c$ from $r=0.5\lambda_0$ until to the droplet center. The density scale length L [$L=(\partial \ln n_e/\partial r)^{-1}$] below the critical density is $0.9\lambda_0$ corresponding to our experimental conditions that the prepulse with a peak-to-pedestal contrast ratio of 10^5 started at about 20 ps at the intensity of 1.1×10^{11} W/cm^2 before the main pulse [24].

Figures 4(a) and 4(b) show the snapshots of longitudinal and transverse component of electric fields E at $60\tau_0$ (τ_0 is the laser cycle) respectively from the 2D PIC simulation for a plasma droplet irradiated by a linearly polarized laser pulse with its polarization along the *y* direction. Laser beam propagates from left to the right. Positions $x=15.0\lambda_0$ and $20.0\lambda_0$ correspond to the front surface (laser-interaction side) and the rear surface of the plasma droplet. From Figs. 4(c) and 4(d) we can see the electric field around the droplet-plasma surface is strongly anisotropic. It is this strong anisotropic electrostatic field that accelerates the protons near the surface of the droplet plasmas and results in an absolutely anisotropic distribution of the fast protons in the polarization plane. Figures 4(c) and 4(e), and Figs. 4(d) and 4(f), show the evolution of the longitudinal and the transverse components of E in a direction crossing the plasma droplet with an angle of 45° [corresponding to the dashed line in (a) and (b)] related to the laser-propagation direction at $50\tau_0$, $60\tau_0$, and $79\tau_0$, respectively. Each plot has three pictures in the same interval of $0.4\tau_0$ at different times. The red, blue, and the green lines indicate the position of the resonance electric field E_r, the quasistatic electric field near the front surface E_{qsf}, and the quasistatic electric field near the rear surface E_{qsr} of the plasma droplet, respectively. From Figs. 4(c)–4(f), we can see clearly the resonance field decreases and the E_{qsf} sustains nearly the same value while the E_{qsr} increases with

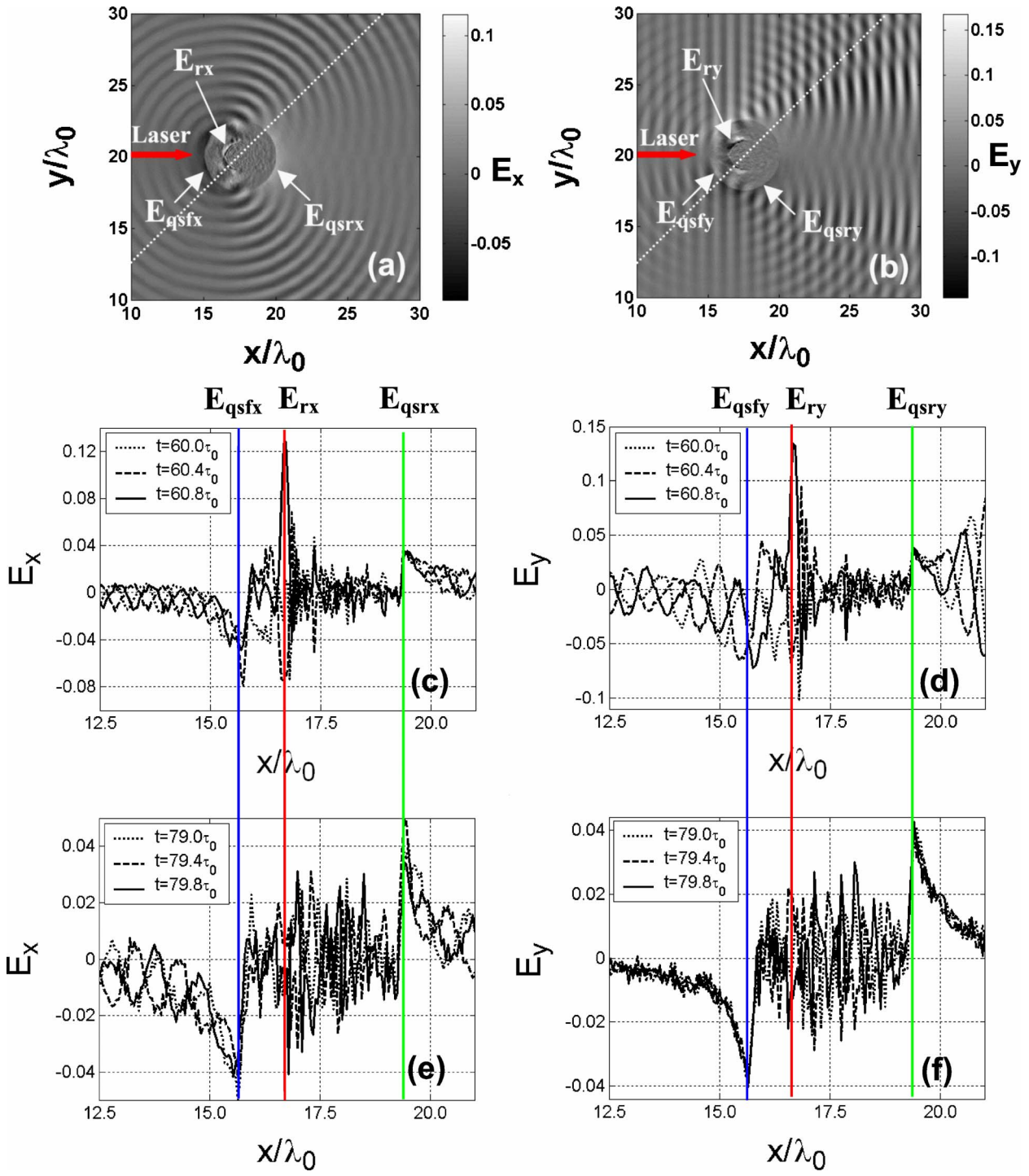

FIG. 4. (Color online) Snapshots of longitudinal and the transverse component of electric fields E at the $60\tau_0$ (τ_0 is the laser cycle) in (a) and (b) respectively from 2D PIC simulation for a plasma droplet irradiated by a linearly polarized laser pulse with its polarization along the y direction. Laser light propagates from left to the right. (c) and (e), (d) and (f) show the evolution of the longitudinal and the transverse components of E in a direction crossing the plasma droplet with an angle of 45° [dashed line in (a) and (b)] related to the laser-propagation direction at $50\tau_0$, $60\tau_0$ and $79\tau_0$, respectively. Each plot has three pictures in the same interval of $0.4\tau_0$ at different time. The red, blue, and the green lines indicate the position of the resonance electric field E_r, the quasistatic electric field near the front surface E_{qsf}, and the quasistatic electric field near the rear surface E_{qsr} of the plasma droplet, respectively.

the time. At $79\tau_0$, the resonance field disappears while the E_{qsr} grows up to the same level as that of E_{qsf}. In addition, from Fig. 4 we can see the maximum of E_{qsf} is larger than that of E_{qsr}. This is well consistent with the experimental result that the back emission of fast protons is stronger than the forward emission, and the maximum energy of protons from the back emission is higher than that of from the forward emission.

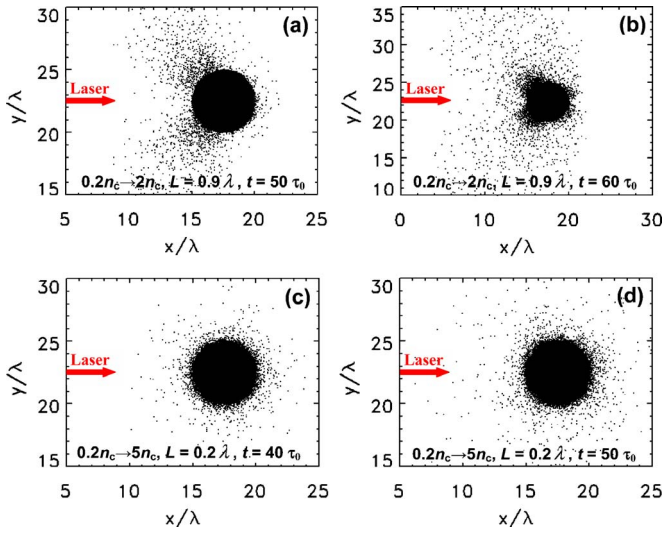

FIG. 5. (Color online) Distributions of hot electrons in the polarization plane of the laser light under different conditions. (a) and (b) represent the typical cases that the resonance absorption dominates in laser-droplet interactions at $50\tau_0$ and $60\tau_0$, respectively. (c) and (d) show the distributions of hot electrons in cases which the vacuum heating dominates in the laser-droplet interactions at $40\tau_0$ and $50\tau_0$, respectively.

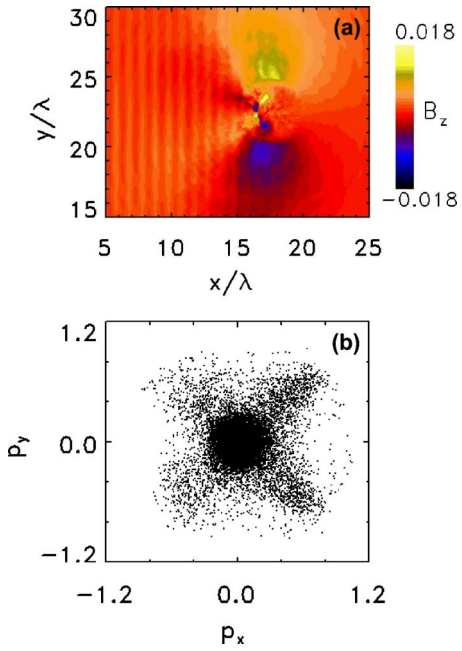

FIG. 6. (Color online) The snapshots of the quasistatic magnetic fields at 50 laser cycles in (a) and the momentum space of electrons at 60 laser cycles in (b), respectively. The simulation conditions are the same as that of in Figs. 5(a) and 5(b).

The accelerating E fields are strongly dependent on the spatial distribution of the "cloud" of the hot electrons. This can be proved by other simulation results of the hot electron distributions at different time shown in Figs. 5(a) and 5(b) corresponding to our experimental conditions described above ($0.2n_c \rightarrow 2n_c$, $L=0.9\lambda$). From Figs. 5(a) and 5(b), we can see clearly that a very strongly anisotropic distribution of hot electrons around the droplet plasma surface. This distribution is due to the anisotropic electrostatic field around the droplet plasma surface in Fig. 4. The anisotropic cloud of electrons around the rear surface appears later than that around the front surface. In our previous work [24], we proved that this anisotropic distribution of hot electrons could be generated mainly by the resonance absorption. In this work, we also run some other simulations under the conditions that the vacuum heating dominates over the resonance absorption. We change the scale length L of the plasmas and the electron density in three cases that initially the electron density increases exponentially along the radial direction of the droplet from $0.2n_c$ at the droplet edge to $10n_c$, $5n_c$, and $2n_c$ at $r=0.5\lambda$ at $40\tau_0$ and $50\tau_0$, respectively. Then we get the distributions of hot electrons in the polarization plane of the laser light. In the first case ($0.2n_c \rightarrow 10n_c$), we can observe an isotropic distribution of hot electrons other than two jets of hot electrons when $L \leqslant 0.4\lambda$. In the second case ($0.2n_c \rightarrow 5n_c$), this situation happens when $L \leqslant 0.2\lambda$. Even in the third case which the density of electrons grows slowly ($0.2n_c \rightarrow 2n_c$), we cannot see an anisotropic distribution of electrons when $L \leqslant 0.2\lambda$. Here we only show the results of the second case in Figs. 5(c) and 5(d) for the sake of simplicity. The above simulations correspond to the conditions that the vacuum heating mechanism dominates in the laser-droplet interaction. These simulations indicate that the vacuum heating mechanism cannot explain a strong anisotropic field around the droplet surface. In addition, from Fig. 5(c) we note that at $40\tau_0$ the hot electron cloud around whole surfaces (including the rear surface) of the droplet is very dense and almost does not change with the time up to $50\tau_0$ [see Fig. 5(d)] in all three cases, while in the case of Figs. 5(a) and 5(b) we cannot observe the dense hot electron cloud around the rear surface until $60\tau_0$. This means that those electrons of the anisotropic cloud around the rear surface are not directly pulled by the laser field.

We notice strong quasistatic magnetic fields around the two jets of hot electrons at 40 laser cycles and get to the highest magnitude at 50 laser cycles as shown in Fig. 6(a) in our PIC simulations under the same simulation conditions as that of in Figs. 5(a) and 5(b). At 50 laser cycles we also observe a quasistatic magnetic field covering the two lateral sides of the droplet. It is possible for this lateral magnetic field to affect the trajectory of the hot electrons and make some electrons go around the target [28]. But this magnetic field always makes the electrons emitting from the lateral sides to have the tendency to drift into the back space around the droplet and to make some electrons go around the droplet into the back space. This means we can exclude the possibility that the lateral electrons go around the target to its rear side (front space) in our case. In addition, since this magnetic field is not strong (the lateral electron current is not so strong in our laser conditions) and it is located in limited space under our experimental conditions, we think this effect is limited. From the momentum distributions of the hot electrons as shown in Fig. 6(b) in our PIC simulations, we observe not only two jets of back-emitting electrons but also two jets of forward-emitting electrons around the critical-density surface of droplet plasma. In fact, those hot electrons with energies over 50 keV can go through an

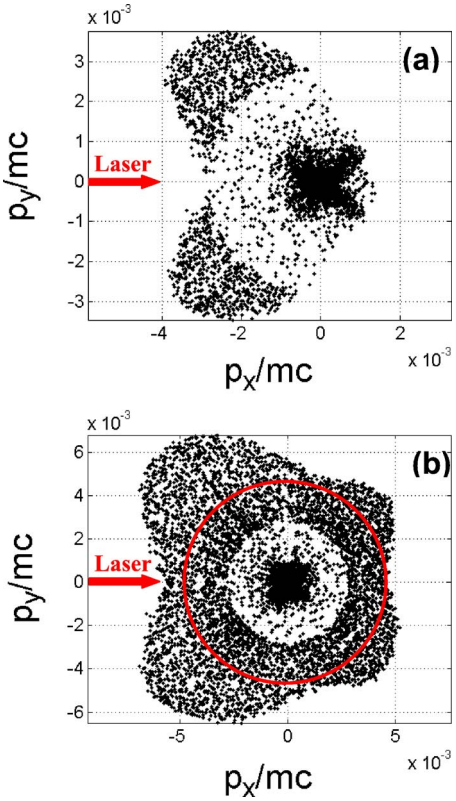

FIG. 7. (Color online) Proton transverse momentum p_y vs longitudinal momentum p_x in the polarization plane of laser light at $60\tau_0$ in (a) and $80\tau_0$ in (b), respectively. The simulating conditions are the same as those of in Figs. 4 and 5.

aluminum film with thickness of 20 μm. The mean size of droplets used in our experiments is 4–5 μm. Therefore, we deduce that some of the hot electrons in these two forward-emitting jets coming from the critical-density surface by the wave breaking due to the resonance absorption going through the droplet target to the rear side, which builds up a space charge and then a sheath forms at the rear surface, and extract protons from the rear side. This mechanism is the so called target-normal sheath acceleration (TNSA) that has been discussed in many papers [1,6,18,19]. Our result is different from that of in Ref. [23], where the authors deduced an anisotropic field around the droplet surface from the measurement of energy spectra of electrons and claimed that those hot electrons were generated by the vacuum heating mechanism.

Figure 7 shows the proton distributions in momentum phase space within the polarization plane of the laser light after different time. At $60\tau_0$ in Fig. 7(a) we can see clearly that two jets of fast protons accelerated by the front field burst out from the front surface of the droplet plasmas. These protons correspond to the group we observed from the back emission of fast protons in Fig. 2(b). This group of protons (we call it the "first group") is continuously accelerated with time and the two jets of protons pulled out by the rear electric field appear clearly at 80 τ_0 [see Fig. 7(b)], while this group (we call it the "second group") has a smaller number than that of from the front surface. At this time, the distribution of the momentum of the protons looks like a "butterfly." In addition, we can also observe a mass of protons with an isotropic distribution of momentums within the red circle in Fig. 7(b) emit in all directions with much slower velocities in 4π space. Apparently this group of protons (we call it the "third group") is independent of the polarization of the laser light, and they are accelerated by the thermal expansion of the droplet plasmas that begins at the irradiance of the prepulse. After the main pulse elapse, both the front and rear electric field decrease and disappear. At this time, the first group and the second group of fast protons get to their highest energies while the third group of slow protons is continuously accelerated due to the hydrodynamic expansion of the droplet plasmas.

With the increase of intensity of the incident laser pulses from weakly relativistic intensity up to relativistic intensity, the distributions of hot electrons and protons display some unique characteristics [29]. The hot electron bunches generated by the laser ponderomotive force separated by a laser period are superimposed to the resonant hot-electron jets and relevant with the hot-electron emission, energetic protons can be separated into two groups.

V. CONCLUSION

We measured directly the angular distributions of protons from few-microns ethanol droplet spray irradiated by linearly polarized 150 fs laser pulses at intensity 1.1×10^{16} W/cm^2. We observed that the fast protons (with energies >16 keV) emitted with an anisotropic distribution only in or near the polarization plane of the laser pulse, while the slow protons (with energies $\leqslant16$ keV) with nearly an isotropic distribution and independence on the polarization state of the laser light emitted at all directions. 2D PIC simulations can reproduce our main experimental results. Simulation results suggest that there are three mechanisms of proton acceleration in the sequence in this laser-droplet interaction: Firstly the first group with highest energies only coming from the back emission is accelerated by the anisotropic charge-separation quasielectrostatic field near the front surface due to the resonance absorption; then the second group coming from the forward emission is generated by the charge-separation quasielectrostatic field near the rear surface built up by the hot electrons from the critical density surface propagating through the droplet; finally, the third group, with the lowest energy, is accelerated by the hydrodynamic expansion of the droplet plasmas. Though both the resonance absorption and the vacuum heating are dependent upon the polarization state of the incident laser light, only the former mechanism can cause an anisotropic electric field around the surface of droplet plasma and an anisotropic distribution of protons.

ACKNOWLEDGMENTS

This research was supported by the National Natural Science foundation of China under Grant Nos. 60321003, 10476033, 10474137, 10574161, and 10374115; the National High-Tech ICF committee; and National Key Laboratory of High Temperature and High Density Plasma.

[1] S. C. Wilks *et al.*, Phys. Plasmas **8**, 542 (2001).
[2] T. Zh. Esirkepov *et al.*, Phys. Rev. Lett. **89**, 175003 (2002).
[3] T. Nayuki *et al.*, Rev. Sci. Instrum. **74**, 3293 (2003).
[4] M. Zepf *et al.*, Phys. Rev. Lett. **90**, 064801 (2003).
[5] T. Fujii *et al.*, Appl. Phys. Lett. **83**, 1524 (2003).
[6] S. Karsch *et al.*, Phys. Rev. Lett. **91**, 015001 (2003).
[7] M. Allen, P. K. Patel, A. Mackinnon, D. Price, S. Wilks, and E. Morse, Phys. Rev. Lett. **93**, 265004 (2004).
[8] L. Romagnani *et al.*, Phys. Rev. Lett. **95**, 195001 (2005).
[9] M. Borghesi *et al.*, Appl. Phys. Lett. **82**, 1529 (2003).
[10] M. Santala *et al.*, Appl. Phys. Lett. **78**, 19 (2001).
[11] M. Roth *et al.*, Phys. Rev. Lett. **86**, 436 (2001).
[12] P. Patel, A. J. Mackinnon, M. H. Key, T. E. Cowan, M. E. Foord, M. Allen, D. F. Price, H. Ruhl, P. T. Springer, and R. Stephens, Phys. Rev. Lett. **91**, 125004 (2003).
[13] A. J. Mackinnon, Rev. Sci. Instrum. **75**, 3531 (2004).
[14] Q. L. Dong, Z. M. Sheng, M. Y. Yu, and J. Zhang, Phys. Rev. E **68**, 026408 (2003).
[15] J. E. Crow *et al.*, J. Plasma Phys. **14**, 65 (1975).
[16] E. L. Clark *et al.*, Phys. Rev. Lett. **84**, 670 (2000).
[17] A. Maksimchuk, S. Gu, K. Flippo, D. Umstadter, and V. Y. Bychenkov, Phys. Rev. Lett. **84**, 4108 (2000).
[18] S. Hatchett *et al.*, Phys. Plasmas **7**, 2076 (2000).
[19] L. Disdier *et al.*, Phys. Rev. Lett. **82**, 1454 (1999).
[20] M. Lezius, S. Dobosz, D. Normand, and M. Schmidt, Phys. Rev. Lett. **80**, 261 (1998).
[21] T. Ditmire, T. Donnelly, A. M. Rubenchik, R. W. Falcone, and M. D. Perry, Phys. Rev. A **53**, 3379 (1996).
[22] S. Busch *et al.*, Appl. Phys. Lett. **82**, 3354 (2003).
[23] D. R. Symes, A. J. Comley, and R. A. Smith, Phys. Rev. Lett. **93**, 145004 (2004).
[24] X. Y. Peng *et al.*, Phys. Rev. E **69**, 026414 (2004).
[25] A. P. Fews and D. L. Henshaw, Nucl. Instrum. Methods Phys. Res. **197**, 512 (1982).
[26] A. P. Fews, Nucl. Instrum. Methods Phys. Res. B **71**, 465 (1992); **72**, 91 (1992).
[27] A. P. Fews, Phys. Plasmas **73**, 1801 (1994).
[28] Amiranoff *et al.*, J. Phys. D **15**, 2463 (1982).
[29] J. Zheng *et al.*, Phys. Plasmas **12**, 113105 (2005).